The effect of aspect ratio on the leading-edge vortex over an insect-like flapping wing

2015 Bioinspir. Biomim. 10 056020

(http://iopscience.iop.org/1748-3190/10/5/056020)

Bioinspiration & Biomimetics

PAPER

The effect of aspect ratio on the leading-edge vortex over an insect-like flapping wing

Nathan Phillips[1], **Kevin Knowles**[2] **and Richard J Bomphrey**[1]

[1] Structure and Motion Laboratory, Royal Veterinary College, University of London, Hatfield, AL9 7TA, UK
[2] Cranfield University, Defence Academy of the United Kingdom, Shrivenham, UK

E-mail: nphillips@rvc.ac.uk

Keywords: leading-edge vortex, flapping wing, micro air vehicle, aspect ratio

OPEN ACCESS

RECEIVED
4 March 2015

REVISED
28 July 2015

ACCEPTED FOR PUBLICATION
30 July 2015

PUBLISHED
12 October 2015

Abstract

Insect wing shapes are diverse and a renowned source of inspiration for the new generation of autonomous flapping vehicles, yet the aerodynamic consequences of varying geometry is not well understood. One of the most defining and aerodynamically significant measures of wing shape is the aspect ratio, defined as the ratio of wing length (R) to mean wing chord ($\bar{c}$). We investigated the impact of aspect ratio, AR, on the induced flow field around a flapping wing using a robotic device. Rigid rectangular wings ranging from AR = 1.5 to 7.5 were flapped with insect-like kinematics in air with a constant Reynolds number (Re) of 1400, and a dimensionless stroke amplitude of $6.5\bar{c}$ (number of chords traversed by the wingtip). Pseudo-volumetric, ensemble-averaged, flow fields around the wings were captured using particle image velocimetry at 11 instances throughout simulated downstrokes. Results confirmed the presence of a high-lift, separated flow field with a leading-edge vortex (LEV), and revealed that the conical, primary LEV grows in size and strength with increasing AR. In each case, the LEV had an arch-shaped axis with its outboard end originating from a focus-sink singularity on the wing surface near the tip. LEV detachment was observed for AR $>$ 1.5 around mid-stroke at $\sim$70% span, and initiated sooner over higher aspect ratio wings. At AR $>$ 3 the larger, stronger vortex persisted under the wing surface well into the next half-stroke leading to a reduction in lift. Circulatory lift attributable to the LEV increased with AR up to AR = 6. Higher aspect ratios generated proportionally less lift distally because of LEV breakdown, and also less lift closer to the wing root due to the previous LEV's continuing presence under the wing. In nature, insect wings go no higher than AR $\sim$ 5, likely in part due to architectural and physiological constraints but also because of the reducing aerodynamic benefits of high AR wings.

1. Introduction

Insects are expert fliers capable of achieving remarkable amounts of lift for their size—often in excess of twice their body weight (Weis-Fogh 1964)—and feats of exceptional aerial agility and control in confined spaces. Flapping flight is also efficient at low flight speeds and in hover (Woods *et al* 2001). Taken together, this flight mode is very attractive for applications to unmanned air vehicles (UAVs). Flapping-wing UAVs take advantage of the unique benefits of insect-like flight and are envisaged for a broad range of applications (Żbikowski 1999) where important characteristics will include energy efficiency, a low audible signature, and the ability to hover and manoeuvre safely in confined and cluttered environments. A better understanding of the fundamental fluid mechanics of flapping wings is essential for informing the design and control of future platforms. A synthesis of the functional consequences of evolved morphologies is also of importance to the biological community where biomechanics can be used to test hypotheses about adaptation and evolutionary radiation.

1.1. Leading-edge vortex

The lift generated by insect wings can be greatly enhanced by leading-edge vortices (LEVs) (Dickinson and Götz 1993), which are similar to the LEVs that form on delta wings, and form when the flow separates due to a large pressure gradient at the sharp leading

edge. It was first observed on flapping wings on a mechanical model by Maxworthy (1979), who also noted the existence of a spanwise flow through the LEV core which transported vorticity into the tip vortex (TiV) effectively keeping the LEV a stable size and in a stable position over the wing surface, thus preventing it from being shed into the wake. Indeed, it has been shown that for a 2D translating wing, the LEV sheds within the first few chords of travel from rest (Dickinson and Götz 1993, Wilkins 2008, Wilkins and Knowles 2009, Garmann and Visbal 2012), while on a revolving wing it has been seen to remain attached even under continual revolutions (Usherwood and Ellington 2002a, Lentink and Dickinson 2009). Since its first observation, the LEV has been observed and characterized on numerous other mechanical flapping-wing models, (Ellington *et al* 1996, Dickinson *et al* 1999, Thomas *et al* 2004, Phillips and Knowles 2013), on live insects (Ellington *et al* 1996, Bomphrey *et al* 2005), as well as on birds (Videler *et al* 2004, Warrick *et al* 2005) and bats (Muijres *et al* 2008), thus, it is a flow feature associated with flapping wings in general. In hovering studies, it is typically observed to have a conical helical structure, where the LEV increases in size towards the wingtip, however, in forward flight it has also been observed to be cylindrical in structure with no detectable helicity (Srygley and Thomas 2002, Thomas *et al* 2004, Bomphrey 2006).

The LEVs that have been described over models often exhibit signs of breakdown, characterized by the formation of a stagnation point on the LEV axis followed by axial flow reversal and a dramatic increase in vortex diameter (Leibovich 1984). Indications of this phenomenon have been reported in numerous studies (van den Berg and Ellington 1997, Lu and Shen 2008, Lentink and Dickinson 2009, Carr *et al* 2013, Phillips and Knowles 2013) and appears to occur at $Re \geqslant \mathcal{O}(10^3)$. It has not been found to impact negatively on lift forces, as it does on delta wings (Lentink and Dickinson 2009). Despite the occurrence of breakdown and formation of smaller vortex structures arising from shear layer instabilities as Re is increased, the general vortex structure and attachment of the LEV is unaffected by changes in Re over the range $200 \leqslant Re \leqslant 60\,000$ (Garmann and Visbal 2012).

1.2. Wing aspect ratio

For conventional fixed wings, the wing aspect ratio, defined as the square of the wingspan divided by the wing area, has a significant effect on the wing's performance. High aspect ratios are more efficient because the average downwash induced by the TiV across the span is lower since local induced downwash varies inversely with distance from the TiV (Anderson 2001). The effect of wing aspect ratio on insect-like flapping wings on the other hand, is relatively unknown but equally likely to impact on aerodynamic performance. Henceforth, we define wing aspect ratio, AR, using a half-span definition: the ratio of wing length R from root to tip, to the mean wing chord $\bar{c}$.

One of the first experimental studies concerning AR effects on insect-like flapping wings was that of Usherwood and Ellington (2002b), who investigated the forces produced by revolving hawkmoth wing planforms in the range AR = 2.27–7.92 held at various fixed angles of attack. They concluded that AR had little effect on force coefficients, but higher aspect ratios saw a steeper growth in lift coefficient with increasing angle of attack. A similar conclusion was reached by Luo and Sun (2005) who used a computational fluid dynamics (CFD) approach to simulate force coefficients in the range of AR = 2.8–5.5. Wilkins (2008) looked beyond this range, simulating an impulsively started rotating wing at 45° angle of attack. The lift coefficient was found to be much smaller for AR = 12.5 compared to AR = 2.5. This was attributed to LEV instability at AR = 12.5 and it was concluded ultimately that AR is critical in dictating LEV stability as it becomes unstable above AR = 10. Beyond this threshold, the LEV repeatedly forms and sheds in the outboard region, resulting in 'cells' of multiple LEVs along the wingspan. This finding concerning LEV stability was supported by a different approach when Lentink and Dickinson (2009) investigated the effects of dimensionless stroke amplitude, Reynolds number and Rossby number (Ro, describing the ratio of inertial to Coriolis forces) using a mechanical model. They simplified the definition of Rossby number—equating it to aspect ratio—and concluded that an LEV will be stable if Ro is of $\mathcal{O}(1)$, implying a stable LEV for AR $<$ 10.

Other experimental work investigating AR effects includes that of Lu *et al* (2006), who investigated flapping wings over the range AR = 1.3–10 and observed the formation of dual LEVs on each wing, concluding that the effect was insensitive to AR. Wojcik and Buchholz (2012) reported the flow field at 25% and 50% span on AR = 2 and 4 wings rotating from rest with a fixed angle of attack, finding higher LEV circulation for the higher AR. Carr *et al* (2013), also investigating AR = 2 and 4 wings rotating with a fixed angle of attack, observed the LEV to be arch-shaped, detaching from the wing surface outboard in both cases. However, the LEV and TiV system for AR = 4 was observed to be less coherent, with the LEV lifting progressively further from the wing than for AR = 2 wings. Furthermore, axial vorticity and velocity levels were reported to be higher in the lower AR = 2 wing. Harbig *et al* (2013) conducted a detailed computational study on AR effects in the range AR = 2.91–7.28 using a numerical model of a fruit fly wing planform swept from rest at a fixed angle of attack of 45°. Visualizations of the flow revealed dual LEV structures with the same sense of rotation for the entire AR range tested. In addition, the higher AR tested was found to achieve lower lift coefficients than the lower ARs at both high and low

'span-based' Reynolds numbers, an alternative definition for *Re* proposed by the authors based on the wing span rather than chord. The only study incorporating AR effects in live insects is that of Henningsson and Bomphrey (2013), who measured the flow around hawkmoths varying in AR from 2.34 to 3.47. The effects on span efficiency (deviation of downwash profile compared to ideal uniform downwash distribution) were examined using time-resolved stereo particle image velocimetry (PIV). Span efficiency varied with normalized lift but inversely with advanced ratio (ratio of free stream velocity to mean wing speed due to flapping), and efficiency values e ranged from 0.31 to 0.6. No effect of AR was reported over the limited range found in hawkmoths, which have a similar planform.

In summary, studies concerning wing aspect ratio effects on flapping wings are limited in number and scope. Moreover, the conclusions are mixed so further investigation is required. The majority of studies have involved a wing at a fixed angle of attack accelerating from rest, rather than reciprocating or flapping. This approach is useful because it simplifies the analysis, isolating AR effects by excluding other effects such as those due to wing pitching. However, in moving towards an understanding of the full complexity of insect-like flapping flight in nature, capturing these effects is essential. Furthermore, only a small number of existing studies have described AR effects on the key flow features (i.e. LEV), and experimental studies are particularly scarce in this area.

1.3. Aims and objectives

The aim of the present study is to characterize the effect of AR on the LEV throughout an insect-like flapping cycle in high spatial resolution using a mechanical flapping device. The advantage of this approach is that it enables precise control of wing geometry and kinematics. We will focus on how the flow field develops throughout the wing stroke, the LEV structure (i.e. position, diameter and circulation), the effects of encountering previously-shed wake, and lift generation. Insect wings range from approximately AR = 1.4 on butterflies to 5.5 on craneflies (Ellington 1984); thus, the chosen range for the present study is AR = 1.5–7.5. The Reynolds number is set at $Re = 1400$, similar to that of a hovering hawkmoth.

2. Materials and methods

2.1. Flapperatus

Insect-like wing flapping was achieved mechanically in the present study using the flapping-wing apparatus known as the 'flapperatus' (figure 1(a)). The flapperatus moves an insect-like wing in air, reciprocating at up to 20 Hz, while enabling separate control of each of the stroke, plunge, and pitch degrees of freedom, thus allowing a wide range of high-fidelity insect-like wing motions. Details on the flapperatus design and operation are published elsewhere (Phillips 2011, 2013). A particular advantage of the device is that it produces very repeatable kinematics up to a 20 Hz flapping frequency, where the wing position in stroke, plunge and pitch is repeatable to within $\pm 0.1^\circ$, $\pm 0.07^\circ$, and $\pm 0.17^\circ$ respectively.

2.2. Coordinate systems

The complex flapping motion of an insect wing can be described by three independent basic motions: stroke (largely fore and aft in hovering flight), plunge (up and down), and wing pitch (angle of attack variation). After Willmott and Ellington 1997, the wing position can be described by the stroke angle ϕ, the plunge angle θ and the pitch angle α, with Φ, Θ, and A denoting their amplitudes as illustrated in figure 2. The present study only considers flight in a hovering condition, thus, the inertial XYZ coordinate system is considered fixed to the insect such that the X-, Y- and Z-axes are aligned with the lateral, forward, and vertical directions respectively as shown in figure 2. Two more coordinate systems are introduced here and are also given in figure 2. The xyz system moves with the wing in the stroke and plunge directions such that the x-axis points in the spanwise direction, the y-axis always remains in the XY plane, and the z-axis is perpendicular to the two. The second $x_w y_w z_w$ frame moves with the wing in all three degrees-of-freedom and is the wing-fixed coordinate system. Here the x_w, y_w, z_w directions correspond to the spanwise (towards wingtip), chordwise (towards the leading edge), and wing upper surface normal directions respectively.

2.3. Test wings and kinematics

The wing planforms investigated comprised a series of rectangular wings with identical chord lengths c of 30 mm, and root-to-tip lengths R ranging from 45 to 225 mm, resulting in aspect ratios of 1.5, 3, 4.5, 6 and 7.5 as shown in figure 1(b). They were designed to be rectangular and rigid so that aerodynamic effects due to changes in AR would be isolated from those relating to shape or flexibility. The justification for maintaining a constant chord length across the cases, rather than constant wing area, was that this allowed for a constant distance of the wing root of 1 chord length from the centre of rotation, which was the minimum distance that could be set due to the design of the mechanism. The wing surface (~0.5 mm thin) was comprised of a carbon fibre composite formed around a 1 mm diameter carbon fibre rod forming the leading-edge spar. The motivation for this material choice and wing construction was that it provided a thin, lightweight and rigid wing.

The wings in this study were dynamically scaled to replicate insect-like flow conditions by choosing a flapping frequency of 1.8 Hz to achieve an insect-relevant Reynolds number of 1400 (similar to a hovering

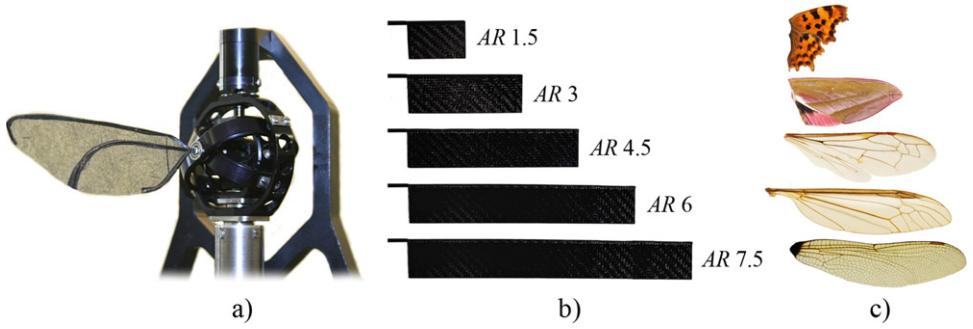

Figure 1. (a) Flapperatus; (b) wing planforms (c) example range of insect wing aspect ratios from ∼1.5 to 6; from top, wings are from *Polygonia c-album*, *Deilephila elpenor*, *Vespula vulgaris*, *Tipula oleracea*, *Aeshna grandis* (forewing).

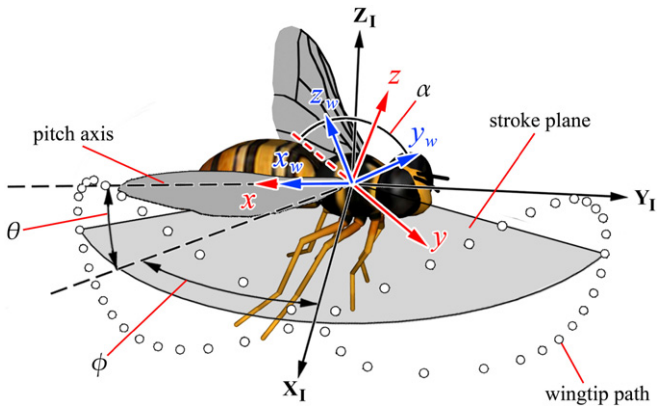

Figure 2. Insect wing position definition and coordinate systems.

hawkmoth). Here, the Reynolds number was based on the constant chord $c = 30$ mm and a constant mean wingtip speed $\bar{v}_{tip} = 0.7$ ms^{-1}. The justification for maintaining a constant mean wingtip speed was that it should ensure a relatively constant TiV strength (thereby keeping TiV effects constant) across the cases, as has been reported elsewhere (Carr *et al* 2013). The dimensionless stroke amplitude, taken as the number of wing chords traversed by the wingtip per wing half-stroke, was fixed at $\Lambda^\star = 6.5$. In insects, $\Lambda^\star$ averages 6.5 and ranges between 1.8 and 10.5 (Weis-Fogh 1973).

Non-dimensional stroke amplitude $\Lambda^\star$ was held fixed, as opposed to fixing the angular stroke amplitude Φ, because flow development has been found to be strongly linked to the number of chords travelled rather than stroke length alone (Ansari *et al* 2008, Granlund *et al* 2010). Here, fixing Φ rather than $\Lambda^\star$ would result in the wingtip on the AR = 7.5 wing traversing 340% further than the lowest AR = 1.5 wing, and thus, the flow would be comparatively more developed outboard on the higher AR wing. It should be noted that in keeping $\Lambda^\star$ and *Re* constant, the angular acceleration profiles across the test cases must change. The lower AR wings experience higher angular accelerations because Φ is larger. However, the linear acceleration profile, in terms of chords travelled at the wingtip, remains constant across the cases, just as the mean wingtip speed does. This translates to a constant Euler fluid force at the wingtip associated with the wing angular acceleration, and acceleration effects are excluded.

The full set of test kinematics are pictured in figure 3 giving the wing stroke, plunge and pitch angles versus time $t^\star$ normalized by the flapping period T throughout one cycle. In addition, the dimensionless stroke position $\lambda^\star$ taken as the number of chords travelled by the wingtip is given. The plunge amplitude was set to zero. The wing's angle of attack was specified to be 45° for 50% of the flapping period with symmetric pitch reversal. These kinematics were chosen because they represent simplified insect-like flapping kinematics that include the essential elements, namely translational phases punctuated by pitch reversal. We excluded variation in wingtip trajectory in an effort to isolate the effect of changing AR within a realistic kinematic parameter space.

In figure 3 the lines represent the measured kinematics output from the flapping mechanism, which can also be thought of as the commanded wing position. Beyond the connection of the wing to the flapping mechanism, a small degree of wing flexion is inevitable, thus, the wing's true position will differ slightly from the position commanded by the flapping

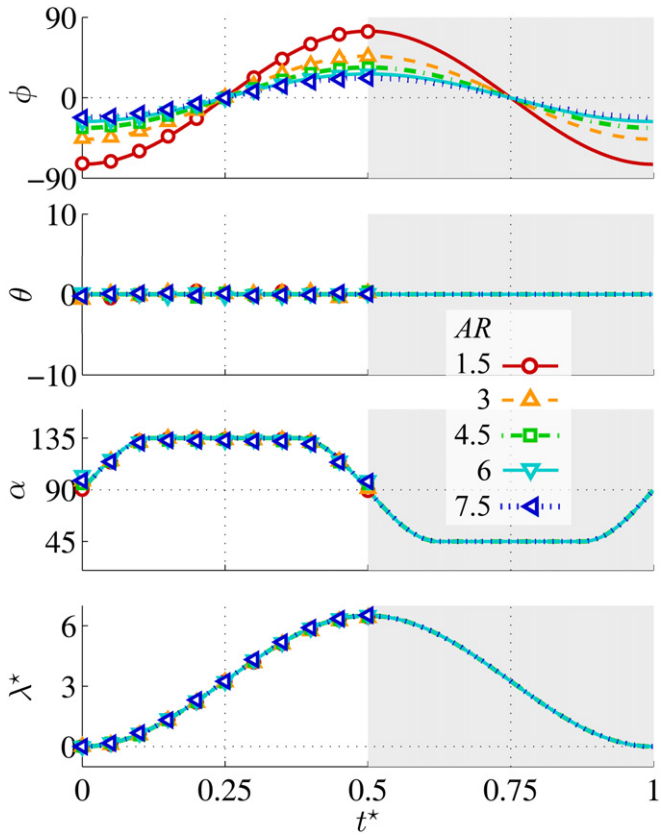

Figure 3. Flapping kinematics throughout flapping cycle for each AR; lines represent measured mechanism output kinematics; symbols represent measured wing position including any wing flexion at the 11 flow field measurement instances; white and grey regions denote separate half-strokes.

mechanism. Wing flexion was measured by manually locating the leading- and trailing-edge positions along the span in the dewarped PIV images, as employed elsewhere (Poelma *et al* 2006, Phillips and Knowles 2013). The actual wing position including flexion is given by the symbols in figure 3 at the 11 measurement instances encompassing one half-stroke. Since the kinematics are symmetric, the flow development between subsequent half-strokes (e.g. downstroke versus upstroke) will also be symmetric, thus, describing the flow development for one half-stroke is sufficient to describe the entire wing stroke cycle. At each measurement instance throughout the half-stroke, flow field measurements were performed at fine increments along the wingspan. The degree of wing twist seen throughout the experimental programme was found to be at worst 3.1° and on average 0.9°, with the wing twisting to a lower angle of attack at the tip. Symbols for α in figure 3 represent the average pitch angle along the span. It should be noted that at stroke reversal, the higher AR wings 6 and 7.5 flexed more in the pitch direction compared to the lower ARs, which is likely a consequence of the greater wing area creating a larger pitching moment and thus more torsional flexion. The kinematic parameters including effects due to wing flexion are given in table 1, where α_{mid} denotes the span-averaged angle of attack at mid-stroke. The errors on these quantities arise, in part, from the uncertainty in manually identifying the leading- and trailing-edge positions, in the dewarped PIV images.

2.4. PIV setup

Flow field measurements were acquired using a high-speed stereo PIV system comprised of a 527 nm 1 kHz Nd:YLF laser (Litron LDY-300PIV, Litron Lasers Ltd, UK) and four 1024 × 1024 px high speed cameras (Photron SA3, Photron Ltd). As illustrated in figure 4, the measurement plane (i.e. the light sheet) was positioned such that it was aligned with the wing chord when the wing was at a pre-defined position in the wing stroke, at which point measurements were triggered by the flapperatus. This enabled repeated measurements and ensemble (or phase-locked) averaging of the flow fields. The light sheet measured ∼1.5 mm in thickness and was produced using a set of optics comprising a spherical and cylindrical lens. Olive oil seeding particles of ∼1 μm in diameter were produced with a compressed air aerosol generator. The laser pulse separation was set such that particles would travel no further than 25% of the light sheet thickness in the out-of-plane direction (previously shown to be optimal (Keane and Adrian 1991)), assuming a maximum out-of-plane velocity of two

Table 1. Kinematic parameters.

AR	Φ (deg)	Θ (deg)	α_{mid} (deg)	$\Lambda^{\star}$ (chords)	f(Hz)
1.5	$147.6 \pm 0.6^{\circ}$	$0.9 \pm 0.6^{\circ}$	$46.0 \pm 0.8^{\circ}$	6.4 ± 0.03	1.8
3	$91.6 \pm 0.4^{\circ}$	$0.9 \pm 0.4^{\circ}$	$46.6 \pm 0.8^{\circ}$	6.4 ± 0.03	1.8
4.5	$67.2 \pm 0.3^{\circ}$	$0.7 \pm 0.3^{\circ}$	$46.4 \pm 0.8^{\circ}$	6.5 ± 0.03	1.8
6	$53.4 \pm 0.2^{\circ}$	$0.5 \pm 0.2^{\circ}$	$47.1 \pm 0.8^{\circ}$	6.5 ± 0.03	1.8
7.5	$44 \pm 0.2^{\circ}$	$0.4 \pm 0.2^{\circ}$	$47.1 \pm 0.8^{\circ}$	6.5 ± 0.03	1.8

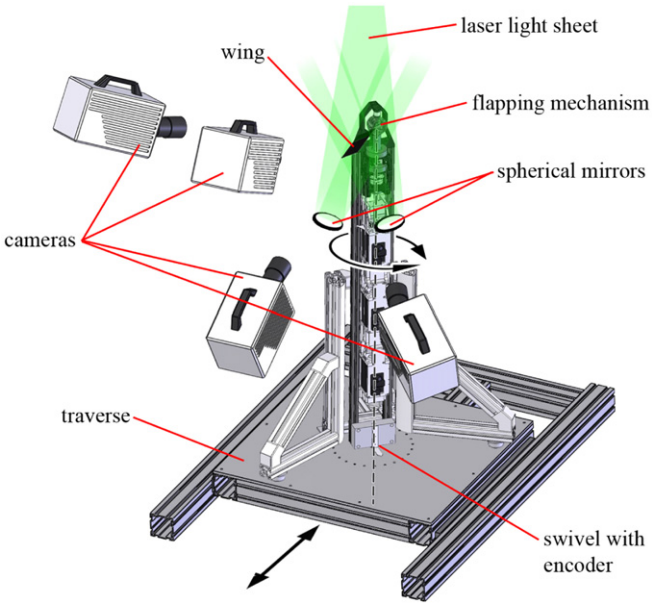

Figure 4. PIV setup with flapperatus.

times the mean wingtip speed that has been reported elsewhere (Lu and Shen 2008, Phillips and Knowles 2013).

Four cameras were used to measure above and below the wing simultaneously (figure 4). To illuminate the shadow cast by the wing, a pair of spherical lenses were arranged ~5 wing chords below the stroke plane to reflect the light sheet onto the underside of the wing. The upper and lower pair of cameras were fitted with 105 mm lenses (AF Nikkor, f/2.8), and 180 mm lenses (AF Nikkor, f/3.5) respectively via Scheimpflug mounts (Westerweel 1997). The PIV system was synchronized with a high-speed controller and operated by DaVis 7.2.2 software (LaVision UK Ltd, Oxfordshire). Spatial calibration of the four camera views was achieved using a dual-plane 105 × 105 mm calibration grid. Small misalignment between the grid plate and the light sheet was corrected with a disparity map routine (Willert 1997, Scarano *et al* 2005).

The flapperatus was mounted on a swivel and a traverse as shown in figure 4. The swivel axis of rotation coincided with the wing stroke centre of rotation, and was fitted with a digital encoder that recorded the swivel angle to within $\pm 0.1^{\circ}$. This enabled measurements at different points in the wing stroke to be achieved without reorienting the PIV measurement frame of reference. The traverse allowed the wing to be translated relative to the measurement plane in 1 mm increments during measurements, resulting in a dense volume of velocity data. The traversing speed was negligible compared to the mean wingtip speed (0.12% of $\bar{v}_{tip}$), nevertheless, following the arrival at a new spanwise location, five flapping periods were allowed to elapse before measurements were resumed. This wait time was found to be more than sufficient such that any effects on the flow field from intermittently traversing the wing were excluded. The resulting measurement volume was comprised of PIV velocity data planes taken every 1 mm from 2 mm inboard of the wing root to 15 mm beyond the wingtip for each wing, with three repeat measures at each spanwise location.

3. Data processing and analysis

3.1. PIV processing

The raw image pairs were pre-processed in DaVis 8.0.8 (LaVision UK Ltd, Oxfordshire) to identify the line of intersection of the laser light sheet with the wing by locating areas above a specified intensity threshold. A mask was applied to this region to exclude it from processing. We calculated a sliding minimum pixel intensity across the image over the three samples taken at each spanwise location and subtracted these

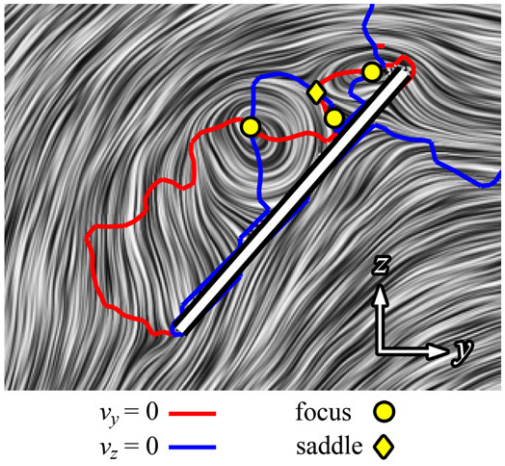

Figure 5. Example automatic critical point identification.

intensities from the individual sample images. This effectively removed reflections from the laser on the wing and background objects, but retained the particle images. Images were subjected to a stereo cross-correlation algorithm with an initial interrogation window size of 64 × 64 px progressing to a final 16 × 16 px window size. For each of these windows, two passes were made with a 50% overlap and deformable windows. Between passes, the median filter proposed by Westerweel (1994) was used to identify and remove spurious vectors, where vector components of twice the rms value of their neighbouring components were considered spurious. After processing, any regions with empty spaces, aside from the masked region, were filled up via interpolation. Vector maps were then averaged over the three samples per spanwise location, and assembled into a dense 3D volume of velocity data for each of the measured instances through the wing stroke.

3.2. Vortex identification

We objectively identified in-plane critical points by locating zero-crossing points for the velocity profiles in the x and y directions (Knowles *et al* 2006). An example is given in figure 5, where intersections between $v_y = 0$ and $v_z = 0$ contour lines mark critical point locations. In this process, critical points are automatically classified into different types (i.e. focuses, saddles) using criteria outlined by Chong *et al* (1990). This technique was applied to every *xy*, *yz* and *xz* plane in the assembled volume of velocity data, resulting in a collection of 3D coordinates of critical points for a given position in the wing stroke. The 3D coordinates of foci were joined into lines representing vortex axes using a custom algorithm exploiting the fact that the 3D vorticity vectors along a vortex axis are tangent to the local path of the axis. With the identified axes, vortex diameter, circulation and axial vorticity were determined at each point along an axis by examining the velocity profile in a plane perpendicular to the local axis direction at a given point. Here the vortex diameter D is taken as the diameter of the rigid-body rotation region in the local Rankine vortex velocity profile, and its circulation is $\Gamma = \pi D v_t$ where v_t is the tangential flow velocity at the extent of the rigid-body rotation region. Details of the employed vortex axis identification method are given elsewhere (appendix, (Phillips 2011)).

3.3. line integral convolution (LIC) and skin friction lines

Flow field velocity measurements were achieved to within ∼1 mm from the wing surface owing to the method we used for filtering out reflections from the wing surface (section 3.1). Without this step, measurements close to the surface are less reliable because the high pixel intensities of the reflections are weighted higher than lower intensities in the correlation function. The reflection removal method effectively reduces them to near-zero pixel intensity leaving only the particles. Measurements near the surface are further complicated by the fact that velocity gradients in the boundary layer lead to bias errors. This has been characterized by Kähler *et al* (2012) who found that bias errors decrease to zero at a distance of one half of the interrogation window size from the surface and beyond. The final interrogation window size used in the present study corresponds to 1.7 mm. Thus, vectors as close as 0.85 mm from the surface are deemed valid and with negligible bias errors. With this in mind, flow velocity measurements at a conservative distance of 1 mm from the wing surface were used to visualize near-surface flows within the boundary layer. The result is a vector field, to which LIC can be applied. LIC was originally presented by Cabral and Leedom (1993), and the method employed here is described in detail elsewhere (Lawson *et al* 2005). Additionally, LIC was applied to chordwise slices through the flow field.

4. Results and discussion

First, we present the 3D flow development versus AR, followed by examination of individual chordwise planes to describe further detail of the LEV diameter and strength. Last, the LEV-generated lift force will be presented and discussed along with corresponding lift coefficient values versus AR.

Figure 6 depicts the formation and evolution of the flow field throughout the wing half-stroke for each AR. The view is of the upper surface of the wing planform, looking down on the wing along the z_w axis in the wing-fixed frame of reference. Near-surface skin friction lines and 3D streamlines released from the core axis mark major vortex structures for AR = 1.5, 3, 4.5 and 7.5 at selected instants throughout the half-stroke. Skin friction lines produced by LIC are coloured by in-plane velocity magnitude normalized by $\bar{v}_{tip}$ and streamlines are coloured with normalized

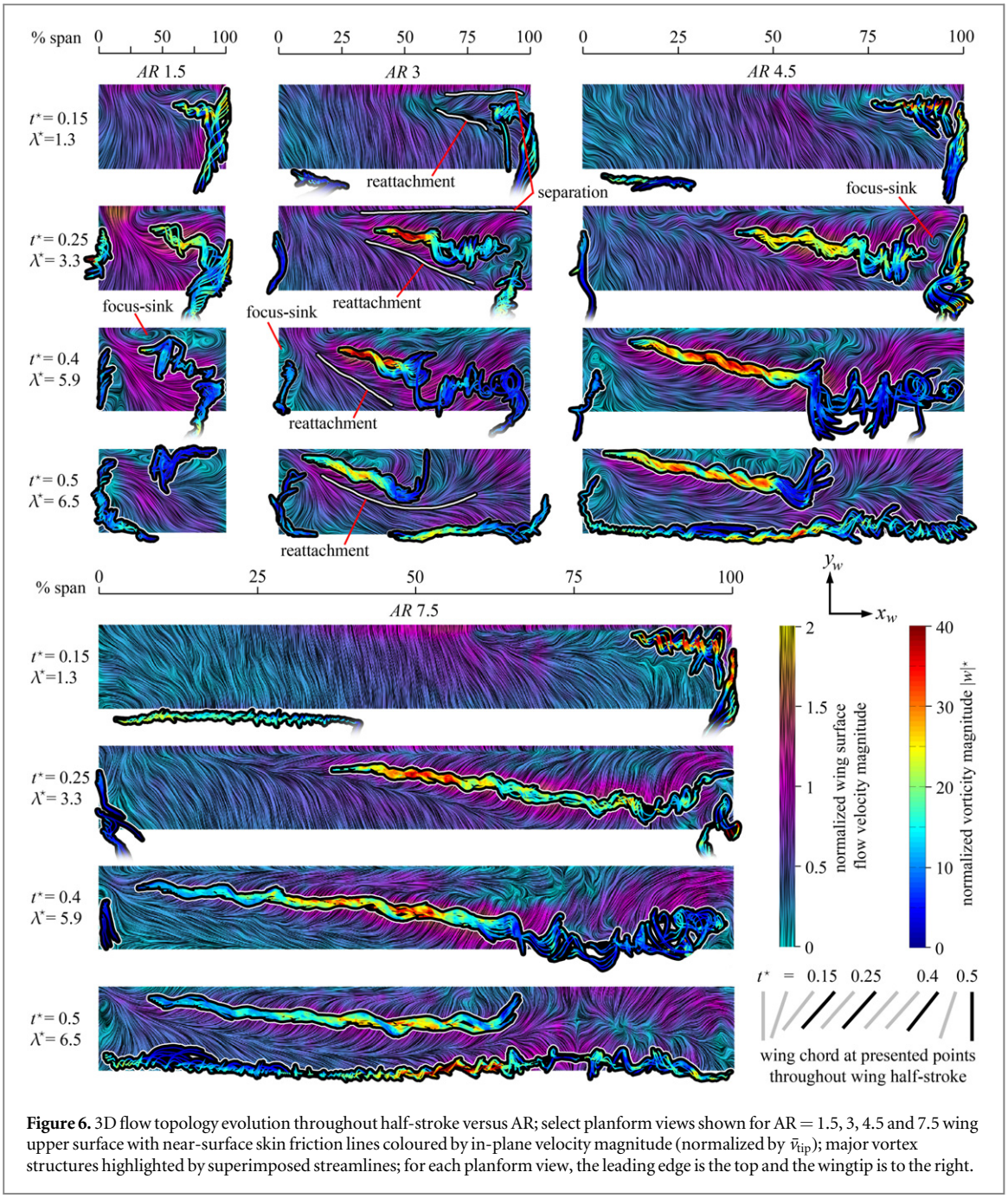

Figure 6. 3D flow topology evolution throughout half-stroke versus AR; select planform views shown for AR = 1.5, 3, 4.5 and 7.5 wing upper surface with near-surface skin friction lines coloured by in-plane velocity magnitude (normalized by $\bar{v}_{tip}$); major vortex structures highlighted by superimposed streamlines; for each planform view, the leading edge is the top and the wingtip is to the right.

vorticity magnitude given by $|w^\star|$. Here vorticity w is normalized by the ratio of $\bar{v}_{tip}/\bar{c}$ ($w^\star = w\bar{c}/\bar{v}_{tip}$).

Complementing figure 6, figure 7 presents the chordwise LEV axis position (figure 7(a)) and height above the wing surface (figure 7(b)) for all ARs at the same instants in the half-stroke.

An interpretation of the flow topologies from the near-surface skin friction lines in figure 6 can be provided by previously established separation patterns. These are derived from local solutions to the Navier–Stokes equations and use critical points such as foci, saddles, sinks and sources (Hornung and Perry 1984, Perry and Chong 1987, Chong *et al* 1990). Such analysis has been applied previously to insect flow topologies by qualitative smoke-wire visualizations (Srygley and Thomas 2002, Thomas *et al* 2004, Bomphrey *et al* 2009), and on flowfield measurements of the LEV growth and detachment process on plunging aerofoils (Rival *et al* 2014). Two of the most common patterns which will be referred to hereon are the open negative bifurcation line separation and the Werlé–Legendre separation illustrated in figure 8 (Hornung and Perry 1984). The former consists of a flow convergence to a separatrix (figure 8(a)), while in the latter, the flow spirals into a focus plus sink (figure 8(b)) where it leaves the surface encircling a vortex axis originating from the focus-sink centre (Hornung and Perry 1984).

4.1. 3D flow development

4.1.1. Early in the half-stroke

As seen in figure 6, the general flow development is qualitatively very similar from AR = 1.5 to 7.5

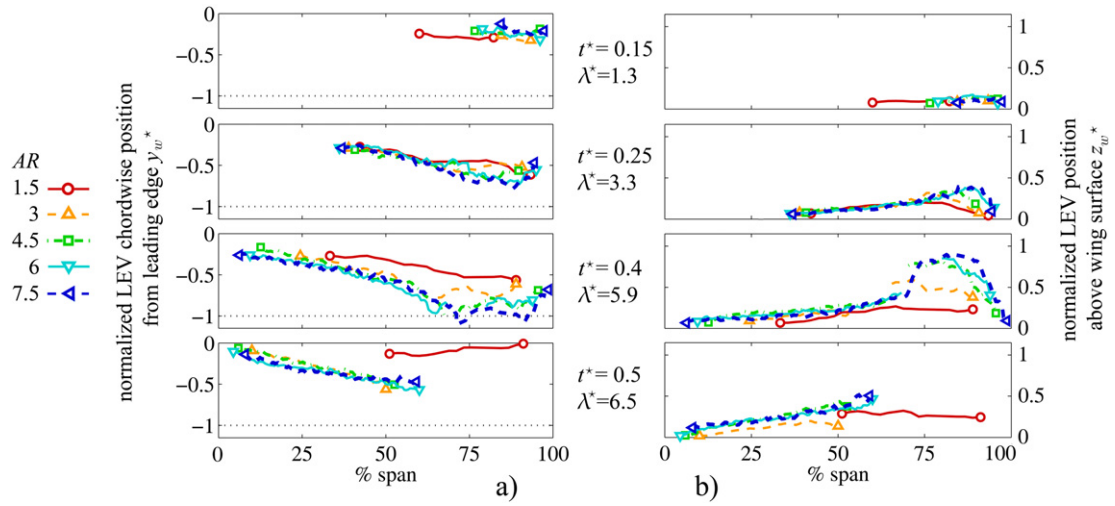

Figure 7. LEV position throughout half-stroke versus AR; (a) chordwise position from leading edge y_w^* and (b) above wing surface z_w^* shown at select points corresponding to figure 6; coordinates are normalized by the wing chord; black dashed line represents the trailing edge.

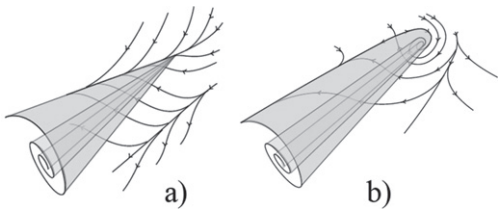

Figure 8. Two common separation patterns adapted with permission from Thomas *et al* (2004); (a) open negative bifurcation line separation; (b) Werlé–Legendre separation.

throughout the half-stroke. At the start of the half-stroke, a trailing-edge vortex (TEV) forms and sheds and the primary LEV first appears outboard around the first 1.3 tip chords of travel ($t^* = 0.15$ see figure 7). At this stage, for all ARs the LEV appears to merge with the TiV and an open negative bifurcation separation line is present close to the leading edge with a reattachment line further aft marking the LEV 'footprint'. For clarity, approximate secondary separation and reattachment lines (see section 3) are marked in figure 6 for AR = 3 only, although the same pattern can be seen throughout the stroke for each AR (with the exception of the end-of-stroke position for AR = 1.5). At $t^* = 0.15$, the remainder of the wing area that is not taken up by the LEV footprint consists of chordwise attached flow directed toward the trailing edge.

4.1.2. Midstroke and after

As the wing proceeds to mid-stroke at $t^* = 0.25$ ($\lambda^* = 3.25$) and beyond to $t^* = 0.4$ ($\lambda^* = 5.9$) at the onset of pitch reversal, the primary LEV continuously grows in size and encroaches further inboard (figure 6). Correspondingly, the reattachment line shifts aft and inboard. Over this period, for higher AR the outboard portion of the LEV axis is generally further from the leading edge and further above the wing surface (figures 7(a) and (b)). This indicates that, outboard, the LEV core position is less stable throughout the stroke as AR increases, possibly resulting in LEV detachment, which will be discussed further in the next section.

The LEV takes an arch-shaped form with its outboard end appearing to be anchored on the wing surface. This is consistent with observations made by Carr *et al* (2013) who reported an arch-shaped LEV for AR = 2 and 4 for a rotating wing at a fixed 45° angle of attack. Our results illustrate that this phenomenon extends up to at least AR = 7.5. The existence of an arch-shaped axis is reinforced by the near-surface skin friction lines in figure 6 which suggest the presence of a focus-sink on the wing surface near the wingtip. From this critical point, the outboard end of the LEV axis emanates. An example of the focus-sink is labelled for AR = 4.5 at $t^* = 0.25$ (figure 6), and similar indications of this feature are seen elsewhere except for AR = 1.5 and 3 at $t^* = 0.4$ where their axes appear less arch-like in figure 7(b).

From the previous observations it appears that prior to mid-stroke, for all ARs the inboard end of the LEV axis originates from an open negative bifurcation line type separation (from the primary separation line along the leading edge) and the outboard end originates from a Werlé–Legendre type separation completing the arch. Post mid-stroke, this remains the case for AR > 3 until the onset of stroke reversal, whereas for AR < 3 the LEV axis outboard becomes continuous with the TiV axis and, thus, has no terminus on the wing surface. Furthermore, for AR = 1.5 an additional focus-sink appears near the leading edge late in the half-stroke (labelled in figure 6), suggesting that for AR = 1.5, the inboard end of the LEV axis transitions to a Werlé–Legendre type separation.

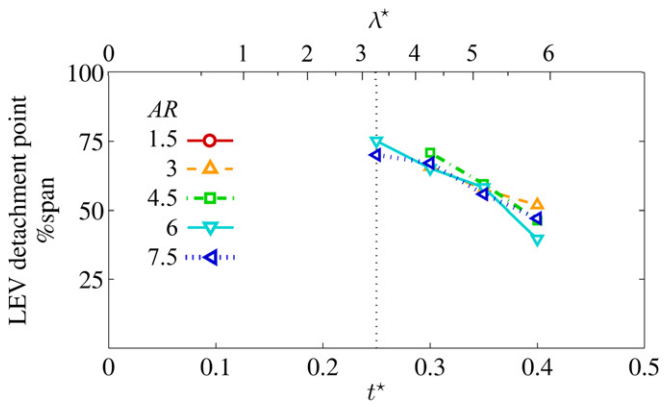

Figure 9. LEV detachment point along span throughout half-stroke versus AR; detachment point is taken as the point where flow reverses at the trailing edge.

Transitional states of separation over hawkmoth wings had been postulated elsewhere (Bomphrey *et al* 2005) and visualized over bumblebees (Bomphrey *et al* 2009); this is further evidence that flow topologies can be highly dynamic throughout the wing stroke cycle.

The trailing vortices also have differing origins, the TiV originates from the open negative bifurcation separation line along the wingtip whereas the root vortex originates from a focus-sink on the wing surface (e.g. AR = 3, $t^\star = 0.4$ in figure 6) and is, therefore, a Werlé–Legendre type separation. It should be noted that a third type of separation pattern referred to as open U-shaped separation is possible for the LEV in which the LEVs on adjacent wings are continuous and extend over the insect's body, as suggested by Luttges (1989) and visualized over insects (Srygley and Thomas 2002, Thomas *et al* 2004, Bomphrey *et al* 2005, 2009, Bomphrey 2006).

4.1.3. LEV detachment

Local LEV detachment in the present study is considered to occur when the flow at the trailing edge reverses and initiates the formation of a TEV. In previous detailed CFD studies by Wilkins (2008), LEV detachment on a translating wing at high angle of attack was seen to be immediately preceded by such a reversal generating a TEV. This is further supported in experimental studies by Rival *et al* (2014) characterizing LEV flow topology, where it was shown that when the stagnation point aft of the LEV merges with the stagnation point at the trailing edge, the merged (saddle) point lifts off the wing initiating LEV detachment. Interrogation of the trailing edge ($\sim 0.03c$ normal distance above trailing edge) throughout the half-stroke for the onset of flow reversal yields the LEV detachment point for each AR as illustrated in figure 9. For the higher ARs, 6 and 7.5, LEV detachment initiates at mid-stroke, at $t^\star = 0.25$, whereas for AR = 3 and 4.5 it occurs shortly after at $t^\star = 0.3$, and no detachment is detected at all for AR = 1.5. Interestingly, despite the wide range in wing length, initial detachment occurs for AR > 1.5 around the same spanwise location of approximately 70% span. This is in close agreement with the numerical simulations of Harbig *et al* (2013) who found that the LEV separates at 70% span over the examined range of AR = 2.91–7.28. In addition, the computational studies of Liu *et al* (1998) reported LEV detachment outboard of a vortex breakdown point at 75% span on a hawkmoth wing. Returning to figure 9, beyond mid-stroke the LEV detachment point progresses inboard at the same rate for each AR (>1.5) until it reaches approximately mid-span at $t^\star = 0.4$, the onset of pitch reversal. Subsequently, the flow reattachment point shifts towards the leading edge due to the influence of the TEV and flow towards the trailing edge is restored along the span. Lentink and Dickinson claimed that the LEV will be continually stable for a revolving wing for *Ro* of $\mathcal{O}(1)$, where *Ro* was equated to aspect ratio, implying the condition of AR of $\mathcal{O}(1)$ for a stable LEV (Lentink and Dickinson 2009). In the present study, all ARs are of this order of magnitude, and our results are consistent with their claims in the sense that the majority of the LEV is stable and remains attached (particularly inboard where the local *Ro* is lower) even up to the end of the stroke. However, the story is more complex, as it is shown here and also elsewhere (Harbig *et al* 2013) that the LEV outboard becomes unstable for AR > 1.5 even though the general condition of AR = $\mathcal{O}(1)$ is met.

4.1.4. End of half-stroke

Finally, beyond $t^\star = 0.4$, the wing pitches up and continues to decelerate until it is at rest at the end of half-stroke ($t^\star = 0.5$; $\lambda^\star = 6.5$). As can be seen in figure 6, for AR > 1.5 a strong TEV is present along the trailing edge at the end of half-stroke, which coincides with pitch reversal. As a consequence of the TEV's presence, the reattachment line migrates toward the leading edge (e.g. AR = 3 in figure 6) such that it lies between the LEV and TEV footprints for

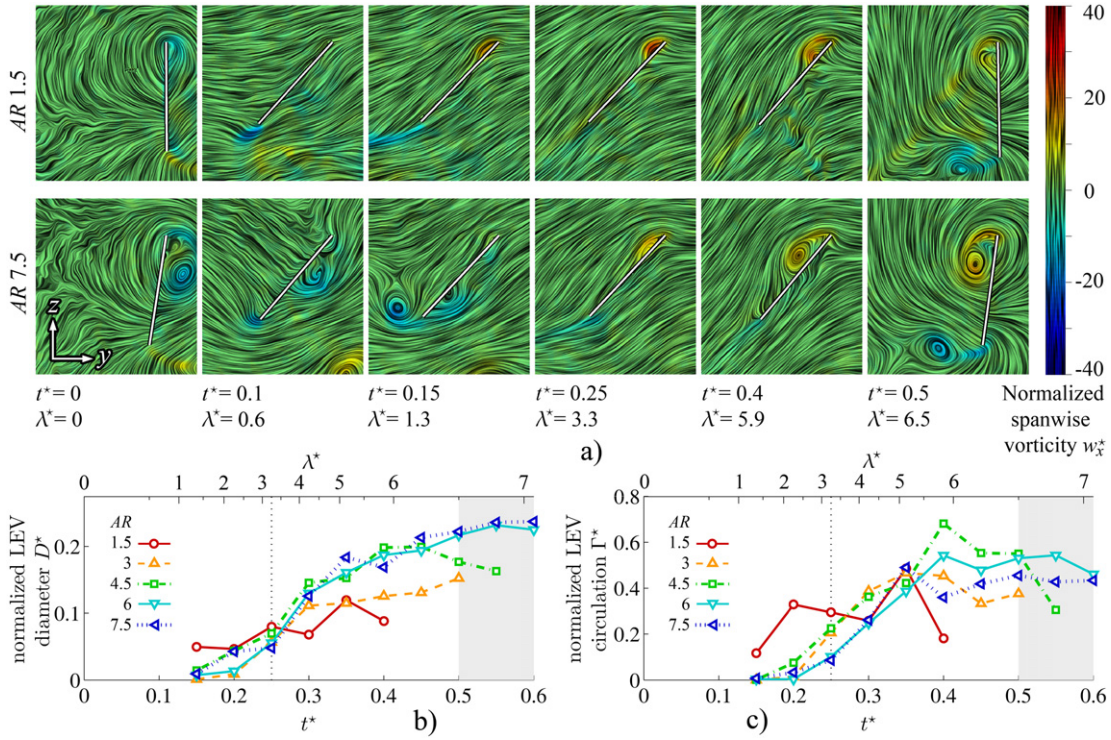

Figure 10. LEV development at 25% span; (a) select chordwise planes of instantaneous streamlines for AR = 1.5 and 7.5; wing chord is denoted by white line; (b) normalized LEV diameter $D^\star$ and (c) normalized LEV circulation $\Gamma^\star$ throughout half-stroke.

AR > 1.5. Also at this stage, no clear LEV axis is found beyond approximately 60% span because the LEV beyond this point has detached and is likely to have broken down. Inboard, however, the LEV position relative to the wing has remained virtually unchanged since $t^\star = 0.4$ (figures 7(a) and (b)). For AR = 1.5 the picture is slightly different at the end of the half-stroke. First, no clear TEV axis is found, probably because the TEV for AR = 1.5 is much smaller and weaker compared to the other ARs. Furthermore, the LEV axis is visible in the outboard region and there is no obvious reattachment line. Compared with $t^\star = 0.4$, the LEV axis for AR = 1.5 has shifted towards the leading edge but is relatively the same distance above the wing (figures 7(a) and (b)).

4.2. Chordwise planes and LEV characteristics

We will now address flow development versus AR by examining chordwise planes through the flowfield along with the LEV diameter and circulation. Figures 10–12 present these results at 25%, 50% and 75% span respectively. Each figure shows chordwise planes of instantaneous LIC streamlines, coloured by normalized spanwise vorticity $w_x^\star$ for AR = 1.5 and 7.5, along with plots of LEV normalized diameter $D^\star$ and circulation $\Gamma^\star$ throughout the half-stroke. Here circulation Γ is normalized according to $\Gamma^\star = \Gamma/(\bar{c}\bar{v}_{\text{tip}})$. In some cases, these plots continue into the next half-stroke (shaded region) where the LEV can be tracked as it persists under the wing into the subsequent half-stroke.

The chordwise planes shown in figures 10(a)–12(a), show again that the general flow development is qualitatively very similar from AR = 1.5 to 7.5. Despite this general similarity there are a number of clear trends that arise as AR increases, which will be outlined below.

First, as AR increases, the primary LEV across the span is generally larger, with stronger circulation. As seen in figures 10(b) and (c) at 25% span it is clearly larger in size in the second half of the half-stroke for higher AR yet normalized circulation values are similar. At 50% span in figures 11(b) and (c) the LEV diameters are more comparable but circulation is higher in the second portion of the half-stroke which implies greater core vorticity for higher AR at this region on the span. Finally, at 75% span, figures 12(b) and (c), the increase in both LEV size and circulation with AR are strikingly clear.

Due to the general increase in LEV size and strength with AR, particularly in the second half of the half-stroke, the inboard portion of the LEV continues to persist under the wing well into the subsequent half-stroke for higher ARs. This can be seen clearly in figure 10(a) at 25% span for AR = 7.5 in approximately the first chord of travel by the wing tip. A similar observation was made by Liu *et al* (1998) who, in a computational study on a hawkmoth wing, saw the LEV deform into a 'hook-shaped vortex' during supination which remained present until the wing began to translate into the upstroke. Furthermore, Poelma *et al* (2006) reported regions of vorticity associated with the

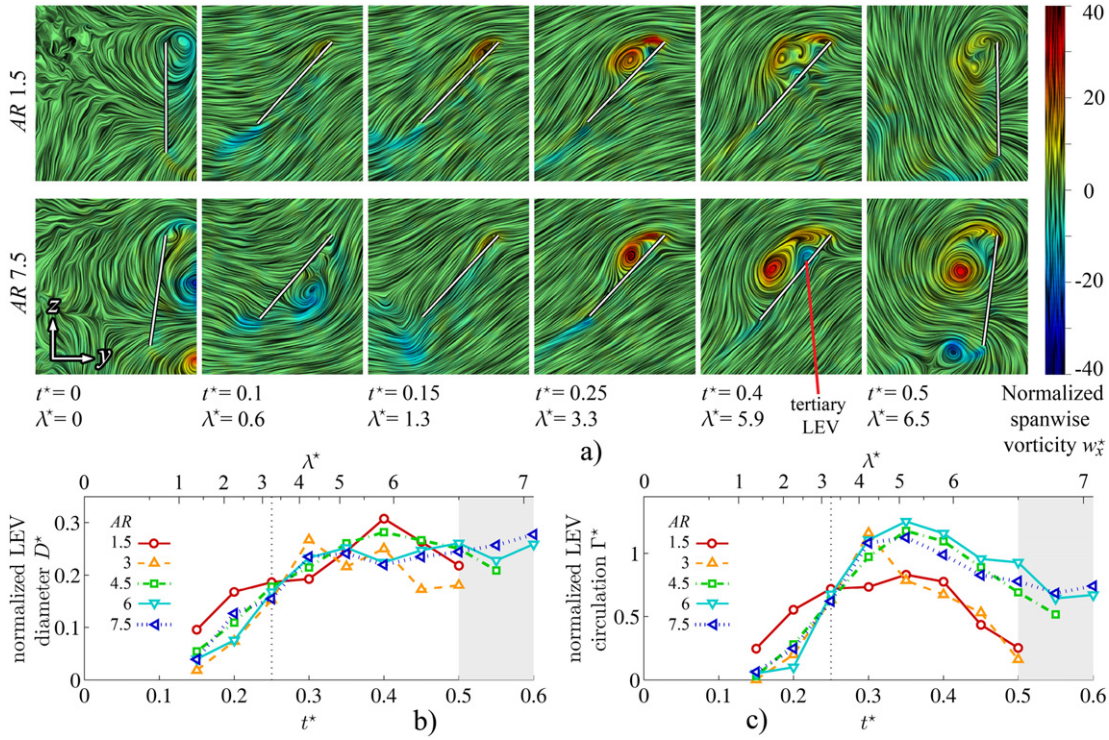

Figure 11. LEV development at 50% span; (a) select chordwise planes of instantaneous streamlines for AR = 1.5 and 7.5; wing chord is denoted by white line; (b) normalized LEV diameter D^* and (c) normalized LEV circulation Γ^* throughout half-stroke

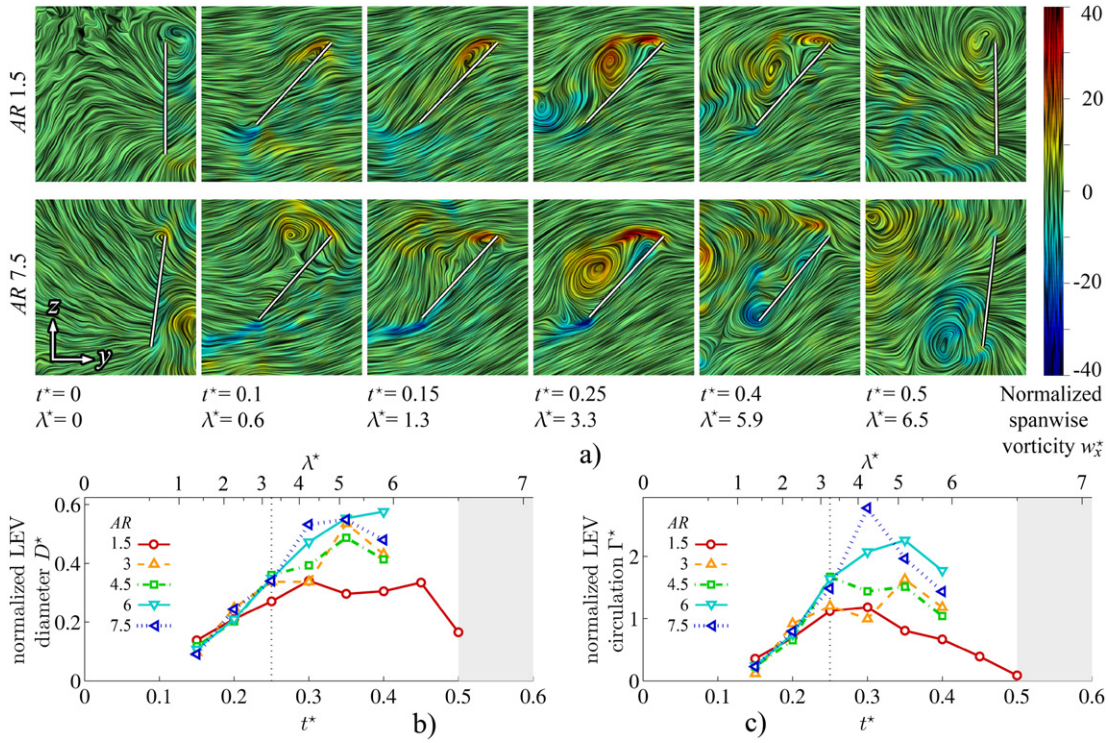

Figure 12. LEV development at 75% span; (a) select chordwise planes of instantaneous streamlines for AR = 1.5 and 7.5; wing chord is denoted by white line; (b) normalized LEV diameter D^* and (c) normalized LEV circulation Γ^* throughout half-stroke.

LEV that convect off the trailing edge during pitch reversal. The persistence of the LEV under the wing will negatively impact lift production into the next half-stroke as it decreases the pressure on the lower wing surface. This negative effect is compounded by the fact that this LEV's presence beneath the wing

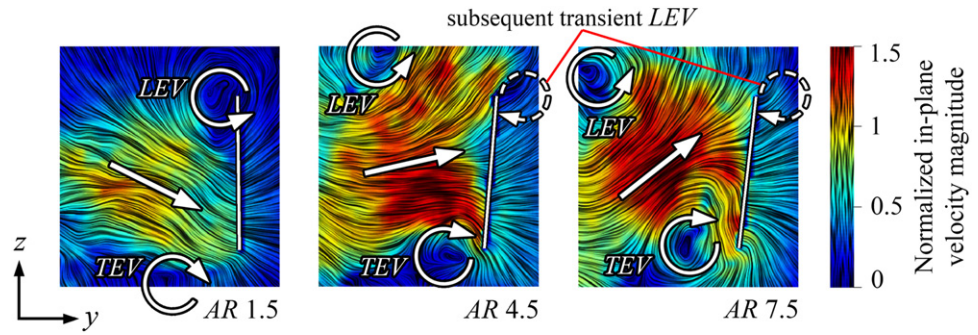

Figure 13. Change in LEV/TEV-induced jet direction (white arrow) with increasing AR; chordwise planes of instantaneous LIC streamlines are illustrated for 75% span at the end of the half-stroke ($t^\star = 0.5$, $\lambda^\star = 6.5$); the wing chord is shown by a white line; in-plane velocity magnitude is normalized by $\bar{v}_{\text{tip}}$.

appears to delay the formation of the new primary LEV, which can be seen by comparing the LEV size and vorticity in the chordwise planes between AR = 1.5 and 7.5 for $t^\star = 0.1$–0.15 at 25% and 50% span in figures 10(a) and 11(a), respectively. The primary LEV forms sooner for the lower AR = 1.5. This is likely to be a result of the fact that the LEV's presence under the wing for a higher AR induces a flow at the leading edge which modifies the direction of the local flow in such a way that the effective angle of attack is reduced and separation is consequently suppressed. The effect can be seen by comparing the direction of incident flow to the leading edge at $t^\star = 0.1$ between AR = 1.5 and 7.5 for 25% and 50% span in figures 10(a) and 11(a), respectively.

The observed delay in LEV formation is also apparent in the trends of diameter and circulation growth at 25% and 50% span (figures 10(b), (c) and 11(b), (c) respectively), where it is seen that for the first half of the half-stroke, the inboard portion of the wing for AR = 1.5 possesses a larger and stronger primary LEV compared to the other ARs. Even though LEV formation is delayed in this manner, the LEV diameter and circulation for higher ARs 'catch-up' as their rates of change are steeper for the first half of the half-stroke and beyond, particularly at the mid-span region.

4.2.1. Secondary and tertiary LEV

In the chordwise planes presented here, additional minor vortex structures are visible that either had no clear 3D vortex axis or were purposely omitted in figure 6. Notably, from approximately mid-stroke onwards in the outboard region, there are indications of a smaller secondary LEV close to the leading edge that has the same sense of rotation as the primary LEV (figures 11(a) and 12(a)). Dual LEVs such as these have been reported on butterflies (Srygley and Thomas 2002) and, as seen from the present results, it is a feature that is present for all ARs. This is consistent with observations by Lu *et al* (2006) who reported dual LEVs with the same sense up to their highest tested aspect ratio of 10, and thus concluded that this flow feature is insensitive to AR. Dual LEVs have been observed numerous times, in both experimental (Lentink and Dickinson 2009), and numerical (Liu *et al* 1998, Harbig *et al* 2013) studies. Furthermore, we have sufficient resolution to observe a tertiary LEV located between the primary and secondary LEVs and with an opposite rotational sense. This occurs at all ARs (for example, at $t^\star = 0.4$ for AR = 7.5 in figure 11(a)). The tertiary structure has been reported by Harbig *et al* (2013) at Reynolds numbers of 750 and above across a range of aspect ratios (2.91–7.28), and elsewhere (Phillips 2011). In delta wing aerodynamics this tertiary vortex is typically referred to as a secondary LEV.

4.2.2. Transient LEV at stroke reversal

At the end of the half-stroke a jet forms between the TEV and the shedding LEV. At lower ARs this jet is directed downwards, while at higher ARs the jet is angled upwards in the outboard region of the wing (figure 13). This shift in jet angle is due to the LEV having convected further away from the wing in the higher AR cases. To compound matters, the TEV is formed earlier in the higher AR cases, which can be seen by comparing $t^\star = 0.4$ between AR = 1.5 and 7.5 in figure 12(a). The TEV is also bigger and stronger towards the end of the half-stroke for higher ARs which, combined with a stronger outboard LEV, creates a greater induced jet between them (figure 13).

As the wing reverses, it is momentarily stationary in the global frame of reference but moving relative to its own induced flow. When the LEV/TEV jet is directed upwards, as it is for our higher AR wings, vorticity can be shed from the leading edge over the new upper surface when the wing speed is zero. This vorticity, which forms on the outboard section of the wing, can be seen in figure 12(a), AR = 7.5, during $t^\star = 0$–0.1, as the wing tip accelerated through its first half chord length of travel. After this shedding event, the primary LEV soon forms. This transient LEV associated with stroke reversal is a flow feature found for AR = 3 and above, and occurs in the outboard region where the

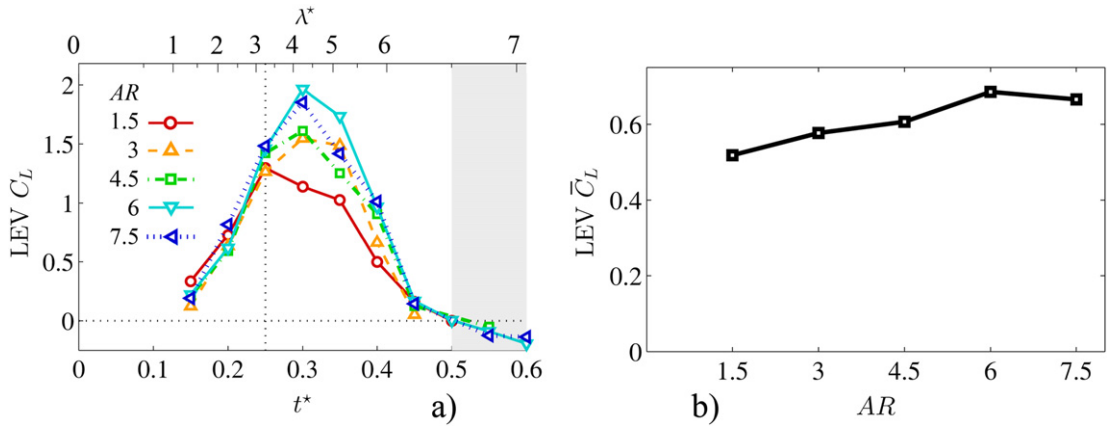

Figure 14. (a) LEV circulatory lift coefficient throughout half-stroke versus AR; (b) time-averaged LEV circulatory lift coefficient versus AR.

primary LEV has already detached. It can be thought of as a form of 'wake capture'. Relatively speaking, the incident flow is directed towards the leading edge in a fashion akin to that experienced by the trailing edge early in the wing stroke when a TEV is generated. Thus, the transient LEV forms and sheds in much the same way that the TEV does at the start of the wing half-stroke.

4.3. LEV lift

The lift generated by an accelerating wing at high angle of attack is the combination of two parts: circulatory lift contained in bound circulation and external vortices, and non-circulatory lift from added mass effects in the acceleration phase. Of the two parts, circulatory lift is more significant as it generates the majority of the lift force throughout a wing stroke (Maybury and Lehmann 2004). In studies by Pitt Ford and Babinsky (2013), it was found that the value for bound circulation that gave the best fit between their potential flow model and experimental flowfield data from a translating wing was small. This led them to the conclusion that the majority of the circulation is contained in external vortices, namely, the LEV. Therefore, the circulatory lift generated by the LEV throughout a wing stroke comprises the majority of the lift produced and, thus, provides a good measure of the total lift.

Here, for a given point in the half-stroke, the circulatory lift of the LEV along the span can be calculated by the varying circulation values along the vortex axis and the local instantaneous wing speed according to the Kutta–Joukowski theorem. The result is a spanwise loading distribution which is then integrated to obtain the lift force and the lift coefficient C_L using $\bar{v}_{tip}$ as the characteristic velocity. We calculated the lift coefficient, using the primary LEV only, for each AR throughout the wing stroke (figure 14(a)). Including the non-circulatory contribution to lift from added mass (Maybury and Lehmann 2004) has a negligible effect because it is comparatively small; for all ARs, the time-averaged lift coefficient from added mass was at most 1.1% of the corresponding circulatory lift coefficient from the LEV.

Lift steadily increases until approximately mid-stroke, and then declines. For the higher ARs (greater than 3), lift forces become negative into the next half-stroke (shaded region in figure 14(a)) as the LEV persists on the wing's underside.

Time-averaged lift coefficients are generally larger for higher AR (figure 14(b)) but this trend does not continue indefinitely. Mean lift steadily increases with AR up to a value of 6 and then declines slightly. The decline in mean lift coefficient at AR $>$ 6 is explained by the drop in LEV circulation after AR $=$ 6 (figures 11(c), and 12(c)). Circulation drops at the highest ARs as the LEV detaches. This phenomenon leads to a higher lift coefficient for AR $=$ 6 than for AR $=$ 7.5 in the latter part of the half-stroke ($t^* > 0.25$; figure 14(a)), and thus, a higher mean value for the entire stroke. Consistent with our results, Harbig *et al*'s computational study (Harbig *et al* 2013) found that for span-based Reynolds numbers $Re_R > \sim 1500$ (c.f. $Re_R = 2500$ here) the mean lift coefficient increases with AR and remains fairly constant in some cases up to a value of approximately 5, after which it decreases. The authors attributed this to a decrease in LEV circulation towards the tip beyond AR $\approx$ 5 which resulted from the interaction with trailing-edge vorticity. The present results show peak lift at AR $=$ 6, whereas in Harbig *et al*'s study lift was seen to decline after AR $=$ 5 (Harbig *et al* 2013). This difference could arise from the different (fruit fly) wing geometry used, and the different approach of characterizing lift using a computational model versus calculating LEV circulation from flow field measurements.

5. Conclusions

The effect of varying wing aspect ratio within, and beyond, the range found in nature was investigated experimentally using high spatial- and temporal-resolution PIV. Qualitatively, the flow fields developed in a similar manner across all wings tested. This was characterized chiefly by the formation of a primary, conical, LEV with an axis that arches above the wing at the outboard end. In most cases, the inboard end of the LEV connected an open negative bifurcation separation line at the leading edge to a Werlé–Legendre focus-sink separation on the wing surface at its outboard end. As the wing half-stroke progressed, the LEV grew in size and strength, with its origin progressing further inboard, forming a larger footprint on the wing surface accompanied by a shift in the flow reattachment line inboard and toward the trailing edge. Also common, was the formation of a secondary LEV closer to the leading edge with the same rotational sense as the primary, and a tertiary LEV located in between the two but with an opposite sense of rotation.

As AR increases, the LEV axis outboard shifts further aft and rises further above the wing surface, the result of a larger vortex diameter outboard that ultimately leads to earlier detachment in this region. Detachment occurred for AR $>$ 1.5 at mid-stroke (initiating earlier with higher AR) at the 70% span location and moved inboard as the half-stroke progressed. Accompanying advanced LEV detachment with increasing AR was the earlier onset of a TEV, even before pitch reversal, due to the influence of the LEV on the flow at the trailing edge. This led to a stronger LEV/TEV vortex pair that was strengthened and reoriented at the end of the half-stroke with higher AR. The consequence of this reorientation is a switch in the LEV/TEV-induced jet to a direction towards the leading edge, which then results in a transient LEV forming on the outboard region of the wing that sheds quickly as the subsequent wing stroke begins.

As a result of the larger and higher LEV circulation across the span with increasing AR, the inboard portion of the LEV (which remains attached) was seen to persist underneath the wing surface into the subsequent half-stroke. This had the effect of reducing lift due to the weakened flow arriving at the leading edge being reoriented in a way that lowered the effective angle of attack and delayed the formation of the primary LEV in the next half-stroke. Thus, the primary LEV forms sooner for lower ARs; however, for higher ARs the rate of growth of its size and strength are steeper and it quickly surpasses the lower ARs as the half-stroke proceeds.

The coefficient of circulatory lift generated by the LEV throughout the half-stroke was found to increase monotonically with AR up to AR $=$ 6, before declining slightly in the AR $=$ 7.5 case. This decline was attributed to a loss in instantaneous lift coefficient in the second half of the wing half-stroke owing to diminished circulation as the outboard LEV sheds. Thus, increasing aspect ratio initially improves lift through a larger and stronger LEV, however the outboard LEV portion grows too large for the wing chord, becomes unstable, and detaches, leading to reduced overall lift. From these results, it appears that the optimal point between these two competing effects is around AR $=$ 6 where peak lift is achieved, at least for a rectangular planform. This could explain why insect wing aspect ratios only go as high as $\backsim$5 (Dudley 1999), because increasing AR to this point improves lift performance. However, further increases in AR provide no aerodynamic benefit to justify the cost of higher inertial power and the higher muscle torques needed to drive the flapping motion.

Acknowledgments

This work was supported by an EPSRC Career Acceleration Fellowship to R J B (EP/H004025/1). The authors would like to thank Dr Graham Stabler for his invaluable advice and help in the development of the experimental apparatus, and Tony Price and John Hogg for their help with installation of the experimental setup. In addition, the authors would like to thank Dr Toshiyuki Nakata for the use of his insect wing images appearing in figure 1(c).

Appendix. Critical point joining algorithm

This appendix describes in more detail the method employed for identifying 3D vortex axes in the measurement volume. Recall from section 3.2 that the method of Knowles *et al* (2006) was used to locate critical points from zero-crossing points of in-plane velocity components. In this process, critical points are automatically classified into different types using criteria outlined by Chong *et al* (1990) for the coefficients P, Q, R from the characteristic equation of the velocity gradient tensor ∇v (i.e. a focus if $Q > 0$, or a saddle if $Q < 0$). In this study, only vortices were of interest, so critical points in the measurement volume not classified as foci were excluded. The remaining points were then joined to form a vortex axis as illustrated by the example in figure A1 using the algorithm outlined subsequently.

The algorithm for joining critical points into a vortex axis requires the user manually to select a starting point, from which the axis is constructed in a step-wise manner. The process will be illustrated by way of an example in 2D. Figure A2 illustrates an axis comprised of points n_1 and n_2, while n_3 and n_4 are being considered for the next axis point. Position and vorticity vectors are given by symbols r and w. Referring to figure A2, for the current point i (n_2) with the previous point being $i-1$ (n_1), subsequent points j(n_3, n_4), must meet the criteria that $r_{j/i}$ (distance to next point)

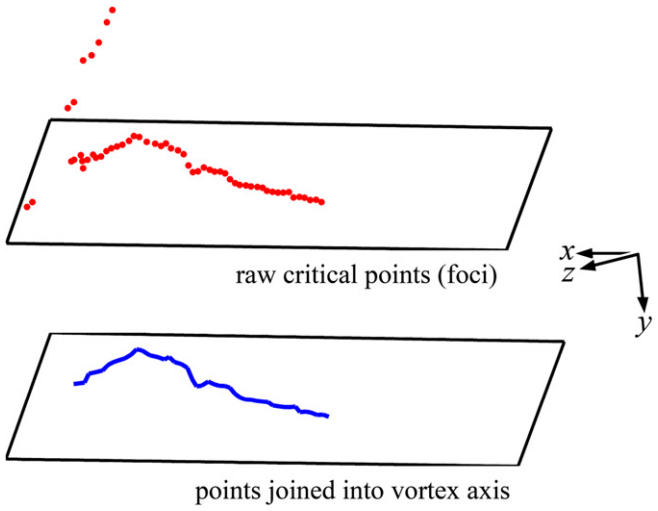

Figure A1. Example result (below) of critical point joining algorithm to form vortex axis (taken from AR = 3 at midstroke).

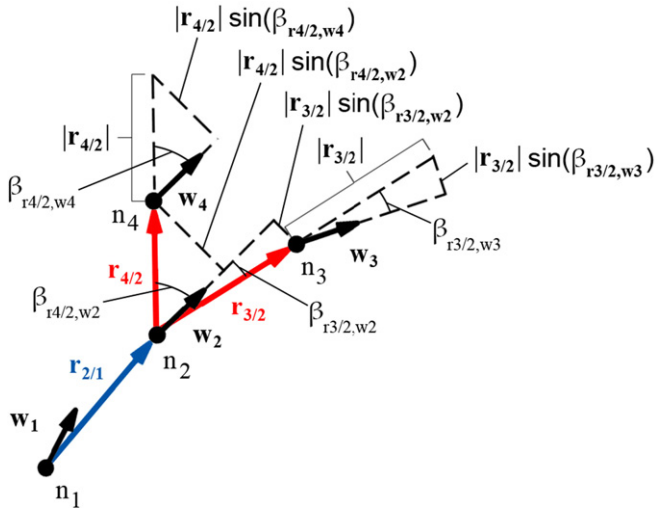

Figure A2. Example step of critical point joining algorithm.

is below 1 mm, and $\beta_{wi,wj}$ (angle between vorticity vectors at point i, and j), $\beta_{rj/i,wj}$ (angle between position vector from i to j and vorticity vector at j), and $\beta_{ri/i-1,rj/i}$ (angle between position vector from $i-1$ to i and position vector from i to j) are each below the threshold of 75°. Of the points that meet these criteria, the one which has the minimum sum of the distances $|r_{j/i}|$, $|r_{j/i}|\sin(\beta_{rj/i,wi})$ and $|r_{j/i}|\sin(\beta_{rj/i,wj})$ is deemed to be the next point on the vortex axis, and the process repeats for the next point. The end of the axis is reached when none of the remaining points meet the initial threshold criteria. These criteria collectively ensure that the deviation of the 3D vorticity vector from the tangent to the local path of the vortex axis is minimized while restricting the vortex axis to turn through a maximum of 75° between subsequent points. Although illustrated using a 2D example, this process was performed in 3D with three-component vectors.

An illustration of the performance of this vortex axis identification method is given in figure A3(a), which presents vorticity vectors along the same identified vortex axis shown in figure A1, where the vectors faithfully follow the axis trajectory. This is made more clear by comparing the axial component of vorticity and vorticity magnitude (which should be equal) along the axis in figure A3(b), indicating the goodness-of-fit of the identified axis to the true axis. Inspiration was drawn from the method of Singer and Banks (1994) which reconstructs vortex axes in a similar stepwise manner using the direction of the current vorticity vector on an axis to step towards the next axis point set at the pressure minimum in a local cross-sectional plane.

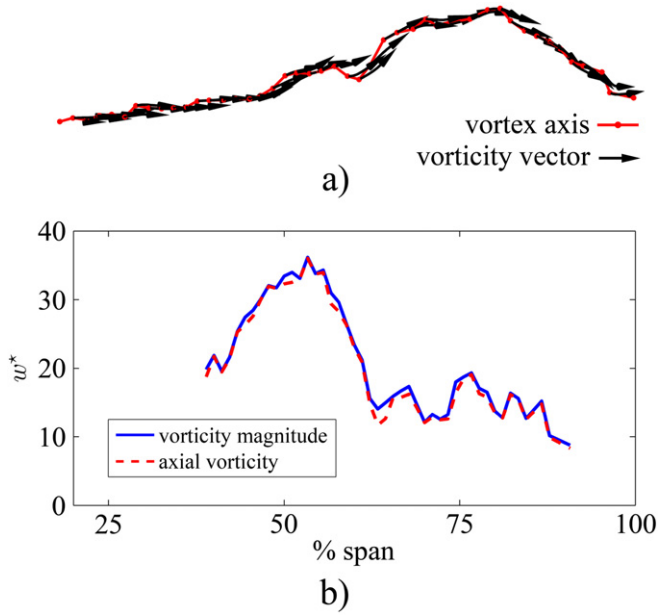

Figure A3. (a) 3D vorticity vectors along vortex axis; (b) vorticity magnitude and axial vorticity along vortex axis.

References

Anderson J D 2001 *Fundamentals of Aerodynamics* 3rd edn (New York: McGraw-Hill)

Ansari S A, Knowles K and Żbikowski R 2008 Insectlike flapping wings in the hover: I. Effect of wing kinematics *J. Aircr.* **45** 1945–54

Bomphrey R J 2006 Insects in flight: direct visualization and flow measurements *Bioinsp. Biomim.* **1** 1–9

Bomphrey R J, Lawson N J, Harding N J, Taylor G K and Thomas A L R 2005 The aerodynamics of Manduca sexta: digital particle image velocimetry analysis of the leading-edge vortex *J. Exp. Biol.* **208** 1079–94

Bomphrey R J, Taylor G K and Thomas A L R 2009 Smoke visualization of free-flying bumblebees indicates independent leading-edge vortices on each wing pair *Exp. Fluids* **46** 811–21

Cabral B and Leedom L C 1993 Imaging vector fields using line integral convolution '*SIGGRAPH 93*' (*Anaheim, US*)

Carr Z, Chen C and Ringuette M 2013 Finite-span rotating wings: three-dimensional vortex formation and variations with aspect ratio *Exp. Fluids* **54** 1–26

Chong M S, Perry A E and Cantwell B J 1990 A general classification of three-dimensional flow fields *Phys. Fluids* **2** 765–77

Dickinson M H and Götz K G 1993 Unsteady aerodynamic performance of model wings at low Reynolds numbers *J. Exp. Biol.* **174** 45–64

Dickinson M H, Lehmann F O and Sane S P 1999 Wing rotation and the aerodynamic basis of insect flight *Science* **284** 1954–60

Dudley R 1999 *The Biomechanics of Insect Flight: Form, Function, Evolution* (Princeton, NJ: Princeton University Press)

Ellington C P 1984 The aerodynamics of hovering insect flight: II. Morphological parameters *Phil. Trans. R. Soc.* B **305** 17–40

Ellington C P, van den Berg C, Willmott A P and Thomas A L R 1996 Leading-edge vortices in insect flight *Nature* **384** 626–30

Garmann D J and Visbal M R 2012 Three-dimensional flow structure and aerodynamic loading on a low aspect ratio, revolving wing *42nd AIAA Fluid Dynamics Conf. Exhibit* (*AIAA New Orleans, Louisiana, USA*)

Granlund K, Ol M, Bernal L and Kast S 2010 Experiments on free-to-pivot hover motions of flat plates *Fluid Dynamics and Co-located Conf.* (Reston, VA: American Institute of Aeronautics and Astronautics)

Harbig R R, Sheridan J and Thompson M C 2013 Reynolds number and aspect ratio effects on the leading-edge vortex for rotating insect wing planforms *J. Fluid Mech.* **717** 166–92

Henningsson P and Bomphrey R J 2013 Span efficiency in hawkmoths *J. R. Soc. Interface* **10** 1–9

Hornung H and Perry A E 1984 Some aspects of three-dimensional separation: I. Streamsurface bifurcations *Z. Flugwiss. Weltraumforsch.* **8** 77–87

Kähler C, Scharnowski S and Cierpka C 2012 On the uncertainty of digital PIV and PTV near walls *Exp. Fluids* **52** 1641–56

Keane R D and Adrian R J 1991 Optimization of particle image velocimeters: II. Multiple pulsed systems *Meas. Sci. Technol.* **2** 963–74

Knowles R D, Finnis M V, Saddington A J and Knowles K 2006 Planar visualization of vortical flows *Proc. Inst. Mech. Eng.* G **220** 619–27

Lawson N J, Finnis M V, Tatum J A and Harrison G M 2005 Combined stereoscopic particle image velocimetry and line integral convolution methods: applications to a sphere sedimenting near a wall in a non-Newtonian fluid *J. Vis.* **8** 261–8

Leibovich S 1984 Vortex stability and breakdown: survey and extension *AIAA J.* **22** 1192–206

Lentink D and Dickinson M H 2009 Rotational accelerations stabilize leading edge vortices on revolving fly wings *J. Exp. Biol.* **212** 2705–19

Liu H, Ellington C P, Kawachi K, van den Berg C and Willmott A P 1998 A computational fluid dynamic study of hawkmoth hovering *J. Exp. Biol.* **201** 461–77

Lu Y and Shen G X 2008 Three-dimensional flow structures and evolution of the leading-edge vortices on a flapping wing *J. Exp. Biol.* **211** 1221–30

Lu Y, Shen G X and Lai G J 2006 Dual leading-edge vortices on flapping wings *J. Exp. Biol.* **209** 5005–16

Luo G and Sun M 2005 The effects of corrugation and wing planform on the aerodynamic force production of sweeping model insect wings *Acta Mech. Sin.* **21** 531–41

Luttges M 1989 Accomplished insect fliers *Frontiers in Experimental Fluid Mechanics* (*Lecture Notes in Engineering* vol 46) ed M Gad-el Hak (Berlin: Springer) pp 429–56

Maxworthy T 1979 Experiments on the weis-fogh mechanism of lift generation by insects in hovering flight: I. Dynamics of the 'fling' *J. Fluid Mech.* **93** 47–63

Maybury W J and Lehmann F O 2004 The fluid dynamics of flight control by kinematic phase lag variation between two robotic insect wings *J. Exp. Biol.* **207** 4707–26
Muijres F T, Johansson L C, Barfield R, Wolf M, Spedding G R and Hedenström A 2008 Leading-edge vortex improves lift in slow-flying bats *Science* **319** 1250–3
Perry A E and Chong M S 1987 A description of eddying motions and flow patterns using critical-point concepts *Ann. Rev. Fluid Mech.* **19** 125–55
Phillips N 2011 Experimental unsteady aerodynamics relevant to insect-inspired flapping-wing micro air vehicles *PhD Thesis* Cranfield University
Phillips N 2013 Three degree-of-freedom parallel spherical mechanism for payload orienting applications *UK Patent* 2464147
Phillips N and Knowles K 2013 Formation of vortices and spanwise flow on an insect-like flapping wing throughout a flapping half cycle *Aeronaut. J.* **117** 471–90
Pitt Ford C W and Babinsky H 2013 Lift and the leading-edge vortex *J. Fluid Mech.* **720** 280–313
Poelma C, Dickson W B and Dickinson M H 2006 Time-resolved reconstruction of the full velocity field around a dynamically-scaled flapping wing *Exp. Fluids* **41** 213–25
Rival D, Kriegseis J, Schaub P, Widmann A and Tropea C 2014 Characteristic length scales for vortex detachment on plunging profiles with varying leading-edge geometry *Exp. Fluids* **55** 1–8
Scarano F, David L, Bsibsi M and Calluaud D 2005 S-PIV comparative assessment: image dewarping+misalignment correction and pinhole+geometric back projection *Exp. Fluids* **39** 257–66
Singer B and Banks D 1994 A predictor-corrector scheme for vortex identification *Technical Report* NASA Contractor Report 194882, ICASE Report No. 94-11 NASA Langley
Srygley R B and Thomas A L R 2002 Unconventional lift-generating mechanisms in free-flying butterflies *Nature* **420** 660–4
Thomas A L R, Taylor G K, Srygley R B, Nudds R L and Bomphrey R J 2004 Dragonfly flight: free-flight and tethered flow visualizations reveal a diverse array of unsteady lift-generating mechanisms, controlled primarily via angle of attack *J. Exp. Biol.* **207** 4299–323
Usherwood J R and Ellington C P 2002a The aerodynamics of revolving wings: I. Model hawkmoth wings *J. Exp. Biol.* **205** 1547–64
Usherwood J R and Ellington C P 2002b The aerodynamics of revolving wings: II. Propeller force coefficients from mayfly to quail *J. Exp. Biol.* **205** 1565–76
van den Berg C and Ellington C P 1997 The three-dimensional leading-edge vortex of a 'hovering' model hawkmoth *Phil. Trans. R. Soc.* B **352** 329–40
Videler J J, Stamhuis E J and Povel G D E 2004 Leading-edge vortex lifts swifts *Science* **306** 1960–2
Warrick D R, Tobalske B W and Powers D R 2005 Aerodynamics of the hovering hummingbird *Nature* **435** 1094–7
Weis-Fogh T 1964 Biology and physics of locust flight: VIII. Lift and metabolic rate of flying locusts *J. Exp. Biol.* **41** 257–71
Weis-Fogh T 1973 Quick estimates of flight fitness in hovering animals, including novel mechanisms for lift production *J. Exp. Biol.* **59** 169–230
Westerweel J 1994 Efficient detection of spurious vectors in particle image velocimetry data *Exp. Fluids* **16** 236–47
Westerweel J 1997 Fundamentals of digital particle image velocimetry *Meas. Sci. Technol.* **8** 1379–92
Wilkins P C 2008 Some unsteady aerodynamics relevant to insect-inspired flapping-wing micro air vehicles *PhD Thesis* Cranfield University
Wilkins P C and Knowles K 2009 The leading-edge vortex and aerodynamics of insect-based flapping-wing micro air vehicles *Aeronaut. J.* **113** 253–62
Willert C E 1997 Stereoscopic digital particle image velocimetry for application in wind tunnel flows *Meas. Sci. Technol.* **8** 1465–79
Willmott A P and Ellington C P 1997 The mechanics of flight in the hawkmoth manduca sexta: I. Kinematics of hovering and forward flight *J. Exp. Biol.* **200** 2705–22
Wojcik C and Buchholz J 2012 The dynamics of spanwise vorticity on a rotating flat blade *Aerospace Sciences Meetings* (Reston, VA: American Institute of Aeronautics and Astronautics)
Woods M I, Henderson J F and Lock G D 2001 Energy requirements for the flight of micro air vehicles *Aeronaut. J.* **105** 135–49
Żbikowski R 1999 Flapping wing autonomous micro air vehicles: research programme outline *14th Int. Conf. on Unmanned Air Vehicle Systems* pp 38.1–38.5